# Extensive marine anoxia associated with the Late Devonian Hangenberg Crisis

Feifei Zhang[1,2,3*], Tais W. Dahl[2], Timothy M. Lenton[4], Genming Luo[5], Shu-zhong Shen[1], Thomas J. Algeo[5,6,7], Noah Planavsky[3], Jiangsi Liu[5], Ying Cui[8], Wenkun Qie[9], Stephen J. Romaniello[10], Ariel D. Anbar[10,11]

[1]*School of Earth Sciences and Engineering, Nanjing University, 163 Xianlin Avenue, Nanjing 210023, China*

[2]*Globe Institute, University of Copenhagen, København K, Denmark*

[3]*Department of Geology and Geophysics, Yale University, New Haven, CT 06511, U.S.A.*

[4] *Global Systems Institute, University of Exeter, Exeter EX4 4QE, UK*

[5]*State Key Laboratory of Biogeology and Environmental Geology, China University of Geosciences, Wuhan, Hubei 430074, China*

[6]*State Key Laboratory of Geological Processes and Mineral Resources, China University of Geosciences, Wuhan, Hubei 430074, China*

[7] *Department of Geology, University of Cincinnati, Cincinnati, OH 45221-0013, U.S.A.*

[8] *Department of Earth and Environmental Studies, Montclair State University, Montclair, New Jersey 07043, USA*

[9] *Nanjing Institute of Geology and Palaeontology, Chinese Academy of Sciences, Nanjing 210008, China*

[10]*School of Earth and Space Exploration, Arizona State University, Tempe, AZ 85287, U.S.A.*

[11]*School of Molecular Sciences, Arizona State University, Tempe, AZ, 85287, U.S.A.*

*Corresponding author: Feifei Zhang
School of Earth Sciences and Engineering,
Nanjing University
163 Xianlin Avenue
Nanjing 210023, China
Tel: +86 17771789784
Email: zhangfeifei414@gmail.com.

**Abstract**

The global Hangenberg Crisis near the Devonian-Carboniferous boundary (DCB) represents one of the major Phanerozoic mass extinction events, which shaped the roots of modern vertebrate biodiversity. Marine anoxia has been cited as the proximate kill mechanism for this event. However, the detailed timing, duration, and extent of global marine redox chemistry changes across this critical interval remain controversial because most of the studies to date only constrain changes in local or regional redox chemistry. Thus, opinions on the significance of anoxia as a kill mechanism are variable—from anoxia being a primary driver to being relatively unimportant. In this study, we explore the evolution of global marine redox chemistry using U isotopes of marine limestones. The $\delta^{238}U$ trends at Long'an section in South China document systematic oscillations with three negative shifts punctuated by two positive events in between. The magnitude of the $\delta^{238}U$ oscillations implies that the sediments do not record contemporaneous seawater with a constant offset at all times. The lack of covariation between $\delta^{238}U$ data and diagenetic indicators (e.g., Mn and Sr contents, Mn/Sr ratio, $\delta^{18}O$) suggests that the $\delta^{238}U$ trends are

not produced by the same post-depositional diagenetic processes. Instead, trace-metal enrichments suggest that more reducing conditions prevailed during the deposition of the two positive events. We present plausible model scenarios that fit the observed δ238U trends in the context of redox-sensitive trace metal data suggesting marine anoxia expanded in the latest Devonian oceans to cover >5% of the continental shelf seafloor area. The rapid expansion of marine anoxia coincident with the onset of the Hangenberg Crisis supports marine anoxia as an important kill mechanism. Biogeochemical modeling of the coupled C-P-U cycles suggests that intensified continental weathering, for example, assisted by the spread of seed plants with deeper root systems at this time, could have triggered expansion of marine anoxia and other global changes (e.g., positive excursion in $\delta^{13}C_{carb}$ and decrease in sea surface temperature) in the latest Devonian. The anoxic event is inferred to have been transient as climatic cooling would have reduced weathering fluxes.

Keywords: Devonian-Carboniferous; mass extinction; Hangenberg Crisis; marine anoxia; uranium isotopes; biogeochemical model

## 1. Introduction

The Late Devonian mass extinction, which occurred in two main phases between 375 and 359 Ma, is one of the "Big Five" mass extinctions in Earth history, marked by a 70–82% extinction rate among marine invertebrate species (Sallan and Coates, 2010). The Late Devonian mass extinction comprised a series of extinction pulses. The main crises occurred at the Frasnian-Famennian stage boundary (~374 Ma) and during the Hangenberg Event close to the Devonian-Carboniferous transition (~359 Ma) (Sallan and Coates, 2010;

70 Becker et al., 2012; Kaiser et al., 2016). Various causes for these extinctions have been
71 proposed, including volcanism, climate change, sea-level changes, global cooling,
72 submarine hydrothermal activity, and/or expansion of marine anoxia/euxinia (e.g.,
73 Joachimski and Buggisch, 2002; Tribovillard et al., 2004; Joachimski et al., 2009; White
74 et al., 2018).

75 Recent work has provided new insights into environmental changes associated with
76 the latest Devonian Hangenberg extinction. Widespread marine anoxia at that time is
77 recorded by globally extensive black, organic-rich mudrock deposition (Algeo et al., 1995;
78 Caplan and Bustin, 1999; Marynowski and Filipiak, 2007; Marynowski et al., 2012; Becker
79 et al., 2016; Kaiser et al., 2016). High-resolution chemostratigraphic studies have provided
80 detailed records of environmental changes in specific regions. In deep-water black shales
81 of central Poland, there is evidence for the development of photic-zone euxinia from green-
82 sulfur bacterial biomarkers (Marynowski and Filipiak, 2007) as well as pyrite framboid
83 size distributions and significant trace metal evidence (Marynowski et al., 2012). In
84 shallow-marine carbonate sections in South China, bulk nitrogen isotope variations suggest
85 locally enhanced nitrogen fixation, possibly as a consequence of increased denitrification
86 in response to expanded marine anoxia (Liu et al., 2016), and I/Ca ratios suggest expansion
87 of the oxygen minimum zone into the ocean-surface layer (Liu et al., in press). There is
88 abundant evidence for redox shifts during the latest Devonian, but all previous studies
89 focused on local or regional redox chemistry changes—in many cases from semi-isolated
90 settings. Therefore, the secular evolution of global marine redox conditions during the
91 latest Devonian remains poorly constrained, despite its importance for understanding
92 global cause-and-effect relationships during the Hangenberg extinction event.

To fill this gap, we investigated the uranium isotope composition of marine limestones (denoted as $\delta^{238}U$), a proxy that can be used to place quantitative constraints on global marine redox chemistry changes (e.g., Dahl et al., 2014; Lau et al., 2016, 2017; Clarkson et al., 2018; Zhang et al., 2018a, b, c; White et al., 2018; Zhang et al., 2019a, b), in the Long'an section, South China, which captured the Hangenberg extinction event. We then used a global uranium cycle model to explore the timing, duration, and extent of global marine redox changes during the Hangenberg extinction event. Finally, we used a global model of C-P-U cycling to test the hypothesis that the spread of seed plants and an associated increased P release could have triggered this event.

## 2. Geological background

The Long'an section is located on the South China Craton, which was situated in the eastern Tethys Ocean close to the equator during the Devonian-Carboniferous transition (Fig. 1). At that time, the southern (paleo-eastern) margin of the South China Craton consisted of a large marine embayment, comprising many shallow carbonate platforms (the Xianggui-Qiangui platform complex) and deep-water troughs of which the Youjiang Basin was the largest. The proximal platforms were attached to the southern margin of the South China Craton, whereas the distal platforms were isolated from land areas by intervening troughs.

The Long'an section is located in Dujie Village of Long'an County in Guangxi Zhuang Autonomous Region (23°10'34.8″ N; 107°27'48.0″ E). The litho- and biostratigraphy of the study section were described in detail by Qie et al. (2015) and Liu et al. (2016). Briefly, the 38-m-thick Long'an section is divided into the Yonghsien and

Long'an formations (Fig. 2). The Yonghsien Formation (−30 to 0 m) consists mainly of massive bioclastic wackestone, packstone, and grainstone, whereas the Long'an Formation (0 to 8 m) is dominated by thin-bedded calcisphere wackestone and packstone. The D–C boundary, which is defined by the first appearance of the conodont *Siphonodella sulcata* (a linear descendant of *S. praesulcata*) is located at ~6 m above the base of the Long'an Formation, and the base of the Upper *praesulcata* and Middle *praesulcata* zones are located at ~2 m and ~3.3 m below the base of the Long'an Formation, respectively (Qie et al., 2015; Liu et al., 2016). Sedimentological evidence (i.e., presence of bioturbation) indicates that the entire study interval was deposited in an oxic shallow-marine setting (Qie et al., 2015), consistent with the study units being passive recorders of seawater U isotope composition with an offset similar to that in modern Bahamian carbonate sediments (Romaniello et al., 2013; Chen et al., 2018).

In this study, 55 nearly pure limestone samples ($CaCO_3$ content from 92.7% to 99.9% with a mean of 98.5%; see Liu et al., 2016) were analyzed for $\delta^{238}U$ and major and trace elements. $\delta^{13}C_{carb}$, $\delta^{15}N_{bulk}$, and I/Ca ratio data from the same suite of samples have been previously reported by Qie et al. (2015), Liu et al. (2016), and Liu et al. (in review).

## 3. Analytical methods

Three to five grams of carbonate powder were dissolved in 1 M hydrochloric acid (HCl) for 24 h at room temperature. Digests were centrifuged and the supernatant was separated. A split of each supernatant was diluted to ~200 ppm calcium (Ca) with 2 % $HNO_3$ and analyzed for a full suite of major and trace element concentrations on a Thermo iCAP quadrupole inductively coupled plasma mass spectrometer (Q-ICP-MS) at the W. M.

Keck Laboratory for Environmental Biogeochemistry at Arizona State University (ASU). Typical precision was better than 3% and 5% for major and trace elements, respectively, based on repeated analysis of in-run standards.

Prior to U purification by ion exchange chromatography, appropriate amounts of $^{236}U$:$^{233}U$ double spike (e.g., Romaniello et al., 2013; Zhang et al., 2018a, b, c; Chen et al., 2018; Zhang et al., 2019a,b) were added to each sample to correct for instrumental and procedural mass-dependent fractionation of the measured $^{238}U/^{235}U$ ratio. The spike-sample mixtures were evaporated to dryness and taken up in 3 N $HNO_3$. Uranium was purified using the UTEVA method (e.g., Romaniello et al., 2013; Chen et al., 2018; Zhang et al., 2018a, b, c; White et al., 2018 for details) before isotopic analysis. All samples were put through UTEVA resin twice in order to completely remove matrix ions. The final purified U was dissolved in 0.32 M $HNO_3$ and diluted to a U concentration of 50 ppb. Uranium isotopes were measured at ASU on a Thermo-Finnigan Neptune multi-collector ICP-MS at low mass resolution. The standard solution CRM145 (50 ppb U) was analyzed every two samples. Two secondary standards CRM129a and Ricca ICP solution were measured after every fifteen measurements. Sample $\delta^{238}U$ values were normalized by the average of the bracketing standards. The $\delta^{238}U$ results are summarized in Figure 2 in the main text and in the *Supplementary Data* file.

## 4. Results

$\delta^{238}U$ values at the Long'an section range from −0.82‰ to +0.32‰ (see Fig. 2 and *Supplementary Data* file). The $\delta^{238}U$ data display a coherent curve with three negative excursions (N1 to N3) separated by two positive excursions (P1 and P2; Fig. 2). The N1

event (a ~0.6‰ negative shift) began in the uppermost Lower *Siphonodella praesulcata* Zone and ended in the lower Middle *S. praesulcata* Zone. The N2 event (a ~1.0‰ negative shift) began in the lower Upper *S. praesulcata* Zone and ended in the upper Upper *S. praesulcata* Zone. The N3 event (a ~0.8‰ negative shift) began in the uppermost Upper *S. praesulcata* Zone and ended in the lower *S. sulcata*-*S. duplicata* zones. Using the measured thicknesses of conodont biozones at Long'an (Qie et al., 2015; Liu et al., 2016, 2018) and the radiometric Devonian time scale of Becker et al. (2012), in which the duration of each conodont zone was calibrated, we calculated an average sedimentation rate of ~37 m/Myr and a total duration of ~1 Myr for the study interval. We are not implying perfectly linear sedimentation, but a total duration of ~1 Myr is supported by a robust biostratigraphic framework.

## 5. Discussion

### *5.1 Evaluation of post-depositional alteration of $\delta^{238}U$ signals in the Long'an section*

The carbonate U isotope redox proxy is a relatively new proxy compared to traditional carbonate C, O, and Sr isotope systematics. Modern carbonate samples from the Bahamas yield $^{238}U$ values with an offset range from 0 to 0.5‰ with an average of 0.27±0.14‰ (1 SD) relative to the overlying seawater (Romaniello et al., 2013; Chen et al., 2018). This offset is generated syndepositionally close to the sediment-water interface (Romaniello et al., 2013). This is a common feature in carbonate sediments, although the redox states of the sediment porewater played an important role (Romaniello et al., 2013), there is still some uncertainty about the processes governing the magnitude of this offset. Samples with evidence for more open-system diagenetic exchange (low Sr/Ca, high Mn/Sr)

185 have been shown to yield slightly greater offsets (Dahl et al., in review). However,
186 diagenetic modeling suggests that preservation of carbonate $\delta^{238}U$ signals should be
187 substantially more robust during fluid exchange than $\delta^{18}O$ and $^{87}Sr/^{86}Sr$ (Lau et al., 2017;
188 Chen et al., 2018), and comparisons of deep drill core samples further confirm that $\delta^{238}U$
189 is not affected to the same degree as $\delta^{13}C$ and $\delta^{18}O$ (Chen et al., 2018; Tissot et al., 2018).
190 In this study, we evaluated potential diagenetic alteration using conventional
191 geochemical criteria. Low Mn contents, high Sr contents, low Mn/Sr ratios, and relatively
192 high $\delta^{18}O$ values are characteristic of carbonate sediments with minimal influence by
193 meteoric diagenesis (e.g., Banner and Hanson, 1990; Jacobsen and Kaufman, 1999; Lau et
194 al., 2016; White et al., 2018; Zhang et al., 2019a). In the Long'an section, Mn contents
195 vary from 11.5 ppm to 90 ppm with a mean of 35 ppm, Sr contents vary from 168 ppm to
196 557 ppm with a mean of 310 ppm, and Mn/Sr ratios vary from 0.03 to 0.33 with a mean of
197 0.12. These characteristics are consistent with well-preserved marine carbonates with
198 minimal chemical alteration during burial diagenesis (e.g., Banner and Hanson, 1990;
199 Jacobsen and Kaufman, 1999; Lau et al., 2016; White et al., 2018; Zhang et al., 2019a; Fig.
200 S1 in the supplementary material). This hypothesis is further supported by O isotope data
201 ($\delta^{18}O$ values > −6‰), which are within the typical range of best preserved Phanerozoic
202 marine carbonate $\delta^{18}O$ values (e.g., Veizer et al., 1999). Therefore, we infer that interaction
203 with meteoric or burial fluids is unlikely to have significantly altered the $\delta^{238}U$ record at
204 Long'an.
205 Changes in lithology—such as dolomitization—are not a concern in the study
206 section. The Mg/Ca molar ratios in the samples are well below 0.01, suggesting negligible
207 dolomitization. Other changes in mineralogy—such as the transformation of aragonite to

208 calcite—can release U into pore fluids. This transformation, however, generally occurs at
209 greater burial depths at which insoluble U(IV) is stable and, thus, any U isotope
210 fractionation in the limestones will be muted or not expressed (Henderson et al., 1999;
211 Romaniello et al., 2013; Chen et al., 2016; Chen et al., 2018). Further, there is no
212 relationship to bulk carbonate Sr/Ca ratios, which are sensitive to aragonite dissolution and
213 Sr capture in secondary calcite phases, which suggests a limited influence from aragonite-
214 to-calcite transition on observed $\delta^{238}U$ trends.

215 Contamination from detrital materials is also not a concern for $\delta^{238}U$ in the study
216 section. Dissolution of carbonate sediments using 1 M HCl has the potential to liberate U
217 from detrital materials. We evaluated this possibility based on Al concentrations and U/Al
218 ratios. Aluminium concentrations range from 8 ppm to 133 ppm with a mean of 39 ppm,
219 confirming that the study samples are relatively pure carbonates with low detrital content.
220 U/Al ratios, which range from 28 to 4114 ppm/wt.%, are significantly higher than the
221 average upper continental crustal value of 0.33 ppm/wt.% (Rudnick and Gao, 2014) or the
222 topsoil mean value of 0.58 ± 1.13 ppm/wt.% (Cole et al., 2017), indicating that our sample
223 digestion protocol has effectively extracted carbonate-associated U. Even if some detrital
224 U was extracted, it is quantitatively insignificant and does not affect the reported $\delta^{238}U$
225 values.

226 Although the analysis above indicates that Long'an carbonates were not strongly
227 altered by post-depositional diagenetic processes, the P1 interval is nonetheless enriched
228 in Fe, Zn, Mo, and U (Fig. 3), suggesting that it was influenced by sulfidic pore fluids in
229 the early diagenetic environment and/or by an input of dissolved metals to the global
230 oceans due to changes in terrestrial weathering. Fe, Zn, and Mo are redox-sensitive

chalcophile metals that accumulate in sediments in which dissolved $H_2S$ is present in pore fluids (Tribovillard et al., 2006). During expansion of marine anoxia, rapid reduction of seawater-soluble U(VI) can lead to massive accumulation of insoluble and isotopically heavier U(IV) below the sediment-water interface. With dissolved $H_2S$ present in sediment pore fluids, isotopically heavy U(IV) can be incorporated into carbonate precipitates. This process has been well documented on the modern Bahamian carbonate platform (Romaniello et al., 2013). Although the overlying water column is well oxygenated, Bahamian sediment pore-waters become sulfidic ~5 cm below the sediment-water interface as a result of abundant organic matter and high rates of respiration and sulfate reduction (Romaniello et al., 2013). We acknowledge that Fe, Zn, and Mo concentrations in carbonates can be biased by the incorporation of terrestrial Fe, Zn, and Mo contributions (i.e., in association with an episode of enhanced terrestrial weathering input). This possibility during the P1 event can, however, be ruled out by the Al normalized elemental plots (Fe/Al, Zn/Al, and Mo/Al; Fig. 3) where stratigraphic spikes in Fe, Mo, and Zn are retained and, therefore, argue for authigenic Fe, Mo, and Zn enrichments during the P1 event. Building from these observations, we suggest that the pronounced U enrichments and the high $\delta^{238}U$ values of the P1 event were most likely a product of strongly reducing pore-water conditions that induced significant authigenic U(IV) enrichments and thus a larger-than-usual early diagenetic offset. This hypothesis has been further modeled in section 5.3. Our study is limited to one section, and we encourage further studies of other sections to assist in disentangling local from global U isotope signals.

In contrast to the P1 event, the P2 event exhibits only Fe and Zn enrichments but no Mo enrichments, although U concentrations are still enriched relative to adjacent

254 sediments. The spikes in Fe and Zn during the P2 event, however, disappears when
255 normalized to Al concentrations (Fig. 3), suggesting that these spikes are mainly associated
256 with a terrestrial input of dissolved metals to the latest Devonian oceans and not driven by
257 local Fe and Zn sulfide precipitation in sulfidic porewaters. Given the fact that Fe, Zn, and
258 Mo sequestration in sediments is strongly enhanced by the presence of free $H_2S$, reductive
259 immobilization of U is less sensitive to $H_2S$ (Tribovillard et al., 2006), the lack of Fe/Al,
260 Zn/Al, and Mo/Al spikes within the P2 interval could indicate anoxic and non-sulfidic
261 pore-water conditions, which led only to small U enrichments (see section 5.3 for further
262 model interpretations). We, however, could not fully rule out the possibility that the P2
263 event represented a global ocean reoxygenation event; this possibility has been modeled in
264 section 5.4 using a C-P-U model, and distinguish between models in section 5.3 and 5.4
265 requires $\delta^{238}U$ measurements from another section.

266 In the modern Bahamas, both bank-top and deep-slope carbonates have $\delta^{238}U$
267 compositions that are heavier than that of contemporaneous seawater by 0–0.5‰ (average
268 of 0.27±0.14‰, 1SD). This offset is not constant and has been attributed to incorporation
269 of $^{238}U$-enriched U(IV) from anoxic pore waters during early diagenesis (Romaniello et al.,
270 2013) or variations in pore-water U-speciation during carbonate recrystallization (Chen et
271 al., 2018). The influence of syndepositional processes on carbonate U are possible because
272 shallow, relatively permeable carbonates can sequester dissolved U(VI) from the overlying
273 oxic water column via advective and diffusive transport. This semi-open system behavior
274 allows an exchange of U isotopes that can induce a net $^{238}U$ offset in bulk carbonate
275 sediments relative to primary carbonate phases. As stated above, this process is not
276 significant at greater burial depths because the mobility of U is severely restricted in anoxic

277 pore fluids, as shown by nearly identical $\delta^{238}U$ offsets in Bahamian carbonates regardless
278 of mineralogy (e.g., aragonite, low-Mg calcite, or dolomite), water depth, and depth below
279 the sediment-water interface (Chen et al., 2018; Tissot et al., 2018). On this basis, we have
280 applied a diagenetic correction factor to measured $\delta^{238}U$ values prior to the U isotope mass
281 balance calculations presented below.
282
283 *5.2 Quantifying marine redox changes using a uranium isotope mass balance model*
284 In order to quantitatively estimate the duration and extent of marine redox
285 variations, we used the U isotope mass balance model of Zhang et al. (2019a) (see also Lau
286 et al., 2016) to calculate the proportion of total marine U burial in anoxic sediments ($f_{anoxic}$)
287 and to estimate the areal extent of marine anoxia in latest Devonian oceans ($A_{anoxic}$).
288 The implied changes to the extent of marine anoxia can be described by differential
289 mass balance equations for the seawater U reservoir and its source and sink fluxes:

290 $$\frac{dN_{sw}}{dt} = J_{river} - J_{anoxic} - J_{other} \quad (1)$$

291 $$\frac{d(N_{sw} \cdot \delta^{238}U_{sw})}{dt} = J_{river} \cdot \delta^{238}U_{river} - J_{anoxic} \cdot \delta^{238}U_{anoxic} - J_{other} \cdot \delta^{238}U_{other} \quad (2)$$

292 $$\delta^{238}U_{anoxic} = \delta^{238}U_{sw} + \Delta_{anoxic} \quad (3)$$

293 $$\delta^{238}U_{other} = \delta^{238}U_{sw} + \Delta_{other} \quad (4)$$

294 Eq. (2) can be rewritten as:

295 $$\frac{d(N_{sw} \cdot \delta^{238}U_{sw})}{dt} = J_{river} \cdot \delta^{238}U_{river} - J_{anoxic} \cdot (\delta^{238}U_{sw} + \Delta_{anoxic}) - J_{other} \cdot (\delta^{238}U_{sw} + \Delta_{other}) \quad (5)$$

296 where $N_{sw}$ is the oceanic uranium inventory in moles, $\delta^{238}U_{sw}$, $\delta^{238}U_{river}$, $\delta^{238}U_{anoxic}$, and
297 $\delta^{238}U_{other}$ are the U isotope compositions of seawater, riverine sources, anoxic sedimentary

sinks, and the average of the remaining other sinks, respectively. $J_{river}$ is the riverine U flux in mol/yr. A $\Delta_{anoxic}$= +0.6‰ is the average isotopic difference between anoxic/euxinic sediments and contemporaneous seawater (e.g, Andersen et al., 2014), and $\Delta_{other}$ is the average isotopic difference between contemporaneous seawater and the remaining other sinks (~ +0.05 ‰, calculated to maintain an isotopic steady state in the modern ocean).

Following prior studies (e.g., Dahl et al. 2014; Lau et al., 2016, 2017; Zhang et al., 2018b; Zhang et al., 2019a), we define $J_{anoxic}$ as:

$$J_{anoxic} = A_{anoxic} \cdot k_{anoxic} \cdot N_{sw} \quad (6)$$

where $A_{anoxic}$ is the total seafloor area overlain by anoxic waters and $k_{anoxic}$ is the rate constant associated with anoxic sediment deposition. Solving equations (1) and (2) at a steady state, we have:

$$f_{anoxic} = \frac{\delta^{238}U_{river} - \delta^{238}U_{sw} - \Delta_{other}}{\Delta_{anoxic} - \Delta_{other}} \quad (7)$$

where $f_{anoxic} = J_{anoxic}/J_{river}$, and the $\delta^{238}U_{SW}$ of the latest Devonian oceans can be estimated using observed $\delta^{238}U$ data for Long'an minus the early diagenetic offset ($\Delta_{offset}$, the $\delta^{238}U$ difference between carbonate sediments and overlying seawater):

$$\delta^{238}U_{sw} = \delta^{238}U_{carb} - \Delta_{offset} \quad (8)$$

Measured carbonate $\delta^{238}U$ for Long'an spans a wide range of values up to +0.2‰. These high values are beyond what can be achieved in open-ocean seawater (where $\delta^{238}U_{sw}$ < –0.28‰ = $\delta^{238}U_{river}$; e.g., Andersen et al., 2017), and therefore these carbonates record seawater with a substantial offset ($\delta^{238}U_{carb}$ – $\delta^{238}U_{sw}$ = $\Delta_{offset}$). A positive $\Delta_{offset}$ is consistent with that observed in drill cores from the modern Bahamian platform (i.e., $\Delta_{offset}$

ranges from 0 to 0.5‰ with an average of +0.27±0.14 ‰, 1 SD; Chen et al., 2018; Tissot et al., 2018). Larger $\Delta_{offset}$ up to +0.6‰ are known to occur in reducing sediments with substantial authigenic U(IV) enrichments (e.g., core 1 from the *T. testudium* flat in the Bahamas; Romaniello et al. 2013). The relatively high $\delta^{238}U$ values in the P1 and P2 intervals imply higher $\Delta_{offset}$ values at those times (i.e., due to anoxic/sulfidic porewater conditions discussed in section 5.1), and these intervals are also characterized by greater U enrichments than other intervals of the Long'an section.

To show that the ocean oxygenation state varied both at the global scale and in the Long'an basin, we first calculated steady state $f_{anoxic}$ values from Eqs. (7) and (8) assuming constant values for $\Delta_{offset}$ of 0‰, +0.27‰, and +0.6‰ (Fig. 4). The other model parameters are given in Table 1. In order to avoid overinterpretation of noise in the $\delta^{238}U_{carb}$ dataset, we interpolated and smoothed measured $\delta^{238}U_{carb}$ values using a LOWESS (LOcally WEighted Scatterplot Smoothing) fit method with a span parameter equal to 0.4. The isotope-driven calculation of $f_{anoxic}$ values shows that the U burial flux into anoxic sediments was significantly greater during the N1, N2, and N3 intervals than today.

All three curves (based on $\Delta_{offset}$ of 0‰, +0.27‰, and +0.6‰) show $f_{anoxic}$ values that are not possible within global U mass balance constraints for some time intervals (i.e., intervals with high $\delta^{238}U_{carb}$ values such as P1 and P2 events; Fig. 4), suggesting that the $\Delta_{offset}$ was not constant and must have varied temporally during accumulation of the Long'an carbonates. We model this possibility by simultaneously changing $A_{anoxic}$ and $\Delta_{offset}$ in Equations (5), (7) and (8) to generate the $\delta^{238}U_{carb}$ trend observed in the Long'an section. Although this approach gives a range of $f_{anoxic}$ solutions for the Long'an dataset, we can nonetheless draw certain conclusions about the solution space. We provided two

342 distinct model scenarios to explain the observed $\delta^{238}U_{carb}$ trend of the Long'an section (Fig.
343 5) that allow higher $\Delta_{offset}$ values at P1 and P2 where elevated Mo and/or U enrichments
344 indicate more reducing pore-water conditions in the early diagenetic environment (Figs. 3
345 and 5).

346 The first modeled scenario (Fig. 5, model scenario 1) started from an oxygenated
347 ocean similar to that of the modern, with the onset of anoxic expansion at the peak of P1
348 (~359.1 Ma). The second scenario (Fig. 5, model scenario 2) started from the same baseline
349 as the first scenario but incorporated an earlier expansion of anoxia (~359.2 Ma) where the
350 U concentration begins to drop. The first modeled scenario fits the $\delta^{238}U_{carb}$ trend of
351 Long'an better, and it also produces a distribution of $\Delta_{offset}$ similar to that observed in
352 modern Bahamian carbonates (Fig. 6), but it fails to mirror the observed U concentration
353 profile. In contrast, the second modeled scenario fits the observed U concentration trend
354 better, but it cannot fully fit the peak of the $\delta^{238}U_{carb}$ trend at P1 because $\Delta_{offset}$ becomes
355 larger than for modern carbonates but is limited to 0.6‰ in our model (Fig. 6). $\delta^{238}U$ offset
356 distribution test supports that our modelled seawater $\delta^{238}U$ curve is realistic, but it does not
357 rule out other plausible seawater $\delta^{238}U$ curves. This will not be resolved until new $\delta^{238}U_{carb}$
358 curves are generated at other sections. Nevertheless, both model scenarios suggest that
359 global marine anoxia expanded significantly, covering >5% of continental shelf areas in
360 the latest Devonian oceans. The maximal extent of marine anoxia is difficult to constrain
361 because modeled $\delta^{238}U$ is insensitive to expanding anoxia once the anoxic U sink
362 dominates other U sink fluxes. However, a >5% expansion of anoxic marine zones is large
363 enough to have extended over most continental shelf areas, which account for just 7.6% of
364 total seafloor area in the modern ocean. The expansion of marine anoxia was coincident

365 with the onset of the Hangenberg Crisis at the base of the Middle *Siphonodella praesulcata*
366 Zone (Fig. 5). The modelled $f_{anoxic}$ curves in Fig. 5 are consistent with the observation that
367 U concentrations overall decrease across the anoxic event in tandem with the changes in
368 I/Ca and nitrogen isotopes (Liu et al., 2016, in press). A full recovery to the pre-expansion
369 background state is, however, not recorded in the studied Long'an section.
370 Both model scenarios can explain the observed P1 and P2 events at the Long'an
371 section by invoking redox changes in the sediment pore-water environment. According to
372 the model, these positive events can be reasonably explained by intensified anoxic/sulfidic
373 conditions in the sediment pore fluids (or in theory the water column above the water-
374 sediment interface based on I/Ca and $\delta^{15}N$ evidence from the Long'an section; Liu et al.,
375 2016, in press), which precipitated $^{238}U$-enriched U(IV) into the Long'an carbonates during
376 the P1 and P2 intervals. For example, our model shows that $\Delta_{offset}$ values must have
377 approached +0.6‰ in the P1 interval and +0.4 to +0.6‰ in the P2 interval (Fig. 5).
378 Our $\delta^{238}U$ data, along with biomarker and other evidence for widespread oceanic
379 anoxia elsewhere globally (Algeo et al., 1995; Caplan and Bustin, 1999; Marynowski and
380 Filipiak, 2007; Marynowski et al., 2012; Liu et al., 2016; Liu et al., in press), confirm that
381 a large proportion of latest Devonian outer continental shelves and upper slopes were
382 covered by anoxic waters. The expansion of marine anoxia would have promoted extensive
383 black, organic-rich mudrock deposition (Algeo et al., 1995; Caplan and Bustin, 1999) and
384 allowed the buildup of $H_2S$ in shallow-water environments (Marynowski and Filipiak,
385 2007; Marynowski et al., 2012). It also increased sediment burial of reduced carbon and
386 sulfur relative to oxidized forms, leading to large positive shifts in $\delta^{13}C_{carb}$ and $\delta^{34}S_{CAS}$
387 globally (Brand et al., 2004; Kaiser et al., 2006, 2008; Qie et al., 2015; Liu et al., 2016).

388

389 *5.3 Testing links of marine anoxia to the spread of land plants and enhanced chemical*
390 *weathering*

391 The Late Devonian was a key interval in the evolutionary history of land plants, as
392 the appearance of the earliest seed plants allowed the spread of terrestrial vegetation into
393 upland areas for the first time (Algeo et al., 1995; Berner et al., 1997; Algeo and Scheckler,
394 1998). This event is thought to have resulted in a decrease of atmospheric $CO_2$ levels and
395 a longer-term increase of atmospheric $O_2$ levels as well as to have had a deep influence on
396 marine biogeochemical cycles (Algeo et al., 1995; Berner et al., 1997; Lenton et al., 2001).
397 The spread of vascular plants and an associated intensification of continental weathering
398 has been proposed to have increased marine phosphorus levels, thus generating higher
399 marine productivity and an expansion of marine anoxic seafloor areas in latest Devonian
400 oceans (Algeo et al., 1995; Algeo and Scheckler, 1998). Intensified continental weathering
401 is supported by an increase in $^{87}Sr/^{86}Sr$ from ~0.70813 to ~0.70829 during the Late
402 Devonian (Brand et al., 2004; McArthur et al., 2012). Conodont apatite oxygen-isotope
403 data imply a concurrent ~3 °C decrease in tropical sea-surface temperatures during the
404 latest Devonian (Joachimski et al., 2009) consistent with more intensive weathering.
405 However, on a million-year time scale, the overall amount of silicate weathering is must
406 be close to be in balance with carbon dioxide outgassing rates, similar to what is observed
407 for the Cenozoic (e.g., Berner and Caldeira, 1997; Caves et al., 2016). In this light, the
408 effect of land plants is likely to change the strength of the silicate weathering feedback or
409 facilitate more efficient P solubilization rather to dramatically change the overall amount
410 of silicate weathering.

To test the hypothesis that the spread of land plants caused the latest Devonian expansion of marine anoxia, we used an existing model of the coupled global C-P-U cycles (Clarkson et al., 2018), slightly updated to use the same U cycle and isotope mass balance as in Section 5.2 (see SI for full model description). We explored various plausible combinations of plant forcing factors to see under what conditions the global model could reproduce the global changes observed in the latest Devonian alongside the global component of the changes in the U isotope record.

We find that a ~33% increase in land plant cover and associated chemical weathering amplification over 200 kyr is capable of generating a transient ~–0.6‰ negative $\delta^{238}U_{sw}$ excursion, a ~2‰ positive $\delta^{13}C$ excursion, a ~3°C global cooling, and an approximate halving of $CO_2$ levels (Fig. 7A). The anoxic fraction of the ocean increases from 0.6% to a maximum of 11%, and the U content of the ocean declines by a factor of ~5× (Fig. 7A). By the start of the P1 event the area of marine anoxia has doubled, and at the peak of P1 it has increased 10×, consistent with our interpretation of a local anoxic signal at this time. Assuming a typical +0.27‰ offset, the initial value of $\delta^{238}U_{carb}$ reasonably matches the mean of the sparse early data (before the N1 event) and the predicted minimum of $\delta^{238}U_{carb}$, and its timing matches the N2 event well (Fig. 7B, green line). Assuming a +0.6‰ offset (blue line), an upper limit on local $\delta^{238}U_{carb}$ matches some but not all of the data for the P1 and P2 events. There are of course large uncertainties in the magnitude of the chemical weathering amplification terms. However, this modeling exercise suggests that reasonable changes in terrestrial realm could drive the observed marine perturbation.

433 The expansion of terrestrial floras during the latest Devonian triggered multiple
434 effects that influenced contemporaneous marine environmental and global climatic
435 conditions. First, expanding terrestrial floras is likely to have enhanced subaerial
436 weathering of phosphorus and increased riverine P fluxes, resulting in increased marine
437 productivity and organic carbon burial (Algeo et al., 1995; Algeo and Scheckler, 1998).
438 The enhanced P delivery may be linked to slow release of organic P during transport of
439 plants to the marine realm. The effects of an increased P flux to the oceans may have been
440 amplified by enhanced phosphorus recycling from marine sediments under anoxic
441 conditions (e.g., Ingall and Jahnke, 1994; Algeo and Ingall, 2007). Second, expanding
442 terrestrial floras increased bulk silicate weathering in the pedosphere through production
443 of root acids, and contributed to increased organic carbon burial through production of
444 refractory organic matter. Collectively, these processes resulted in sharp declines in
445 atmospheric $CO_2$ and temperatures during the Late Devonian (Berner, 2006; Algeo and
446 Scheckler, 2010). However, feedbacks with the weathering-climate system tended to limit
447 the duration of such events. For example, deep weathering of soils slowly reduces the rate
448 of liberation of new P (Algeo and Scheckler, 1998), and release of oxygen through organic
449 carbon burial slowly ventilates anoxic marine systems, limiting phosphorus recycling
450 effects (Algeo and Ingall, 2007). In our model, the oceanic anoxic event (OAE) ceased
451 after a total duration of ~400 kyr. This produced a recovery in $\delta^{238}U_{sw}$ to more positive
452 values resembling the N2 to P2 transition, thus suggesting that the P2 event was not
453 necessarily a local sedimentary signature.
454 There may have been several pulses of enhanced weathering and expansion of
455 marine anoxia during the Late Devonian. The coupled C-P-U model with biogeochemical

feedbacks (Fig. 7) predicts that a single episode of terrestrial floral expansion would have generated a transient expansion of marine anoxia. In contrast, the $f_{anoxic}$–$\Delta_{offset}$ models (Fig. 5) suggest that expansion of marine anoxia would have been globally more persistent. In order to generate a second expansion of marine anoxia in the C-P-U model (and match the N3 data), a second episode of terrestrial floral expansion can be invoked, but again the consequences would have been transient. Given the short duration of our $\delta^{238}U_{carb}$ record and uncertainties surrounding its interpretation in terms of global and local signals, we think it premature to propose too precise of an environmental history. Nonetheless, it is encouraging that the C-P-U model can simultaneously generate several of the global changes observed in the latest Devonian, consistent with the hypothesis that the spread of land plants caused at least one transient oceanic anoxic event at this time.

*5.4 Marine redox changes and the Hangenberg extinction*

Current data support a prolonged duration for the Hangenberg biotic crisis, lasting from the onset of deposition of the Hangenberg black shale in the latest Devonian into the earliest Carboniferous (Kaiser et al., 2008, 2011). The main phase of the Hangenberg Crisis occurred at the base of the Middle *praesulcata* Zone, a level marked by declines in conodonts, ammonoids, trilobites, stromatoporoid sponges, corals, brachiopods, bivalves, and various marine phytoplankton (e.g., Caplan and Bustin, 1999; Kaiser et al., 2016). Climatic cooling and global sea-level changes have been cited as causes of the Hangenberg crisis (e.g., Kaiser et al., 2016), although the pattern of sea-level change during this critical interval is under debate (Johnson et al., 1985; Algeo et al., 2007; Qie et al., 2015; Kaiser et al., 2016). Furthermore, sedimentological evidence shows that there were sea-level

fluctuations before and after deposition of the Hangenberg black shales (Walliser, 1984; Johnson et al., 1985), so a direct role for sea-level changes in the biotic crisis is doubtful. Here, our new $\delta^{238}U$ data highlight that, apart from any changes in sea-surface temperatures and sea-level elevations, the expansion of marine anoxia in latest Devonian oceans is likely to have been a key factor triggering stresses among marine organisms and communities. The expansion of marine anoxia in the upper Lower *Siphonodella praesulcata* Zone coincided with the onset of the Hangenberg biocrisis. This expansion of anoxia was vast enough to have plausibly bathed the outer continental shelves and upper slope areas (i.e., when compared to a situation in the modern oceans where the shelf occupies ~7% of the total ocean floor).

## 6 Conclusions

We studied $\delta^{238}U$ variations in limestones from the latest Devonian to the earliest Carboniferous in the Long'an section of South China, which preserves a record of the global Hangenberg Crisis. This is the first $\delta^{238}U$ record for the Hangenberg Crisis. The $\delta^{238}U$ profile of the study section shows large secular variations with three negative excursions separated by two positive excursions. We suggest that these positive events are best explained by intensified anoxic/sulfidic conditions in pore fluids during U uptake, which captured $^{238}U$-enriched U(IV) in the Long'an carbonates. U isotope mass balance calculations suggest that global marine anoxia expanded strongly in latest Devonian oceans, covering >5% of total global seafloor area and potentially the majority of contemporaneous continental shelves. The expansion of marine anoxia in the upper Lower *praesulcata* Zone coincided with the onset of the Hangenberg Crisis, consistent with a central role for marine

anoxia in triggering the extinction event. Global modeling of the coupled C, P, U cycles shows that the spread of seed plants and an associated increased continental to marine P flux could have triggered expansion of marine anoxia in latest Devonian oceans and other global changes, including the positive $\delta^{13}C_{carb}$ excursion and global cooling at that time, but the expansion of anoxia is predicted to have been transient as P solubilization rates and overall weathering intensities declined through internal feedbacks.

**Acknowledgments**

F.Z. and T.W.D. acknowledge support from the Danish Council for Independent Research (No. DFF 7014-00295). T.W.D. acknowledges support from the Carlsberg Foundation (grant number CF16-0876). S.Z.S.'s work is supported by the Strategic Priority Research Program (B) (XDB26000000, XDB18000000). T.M.L. was supported by NERC (NE/P013651 and NE/N018508/1). NJP acknowledges funding from the Packard Foundation. Y.C. is supported by internal grant from Montclair State University and the National Science Foundation of China (Grant 41888101). F.Z. and A.D.A. acknowledge funding from the NASA Astrobiology Program (award NNX13AJ71G) and the NSF Frontiers in Earth System Dynamics program (award EAR-1338810).

**REFERENCES**

Algeo, T.J., Ingall, E., 2007. Sedimentary $C_{org}$:P ratios, paleocean ventilation, and Phanerozoic atmospheric $pO_2$. Palaeogeogr. Palaeoclimatol. Palaeoecol. 256 (3), 130–155.

Algeo, T.J., Scheckler, S.E., 1998. Terrestrial-marine teleconnections in the Devonian:

525 Links between the evolution of land plants, weathering processes, and marine anoxic
526 events. Roy. Soc. London Phil. Trans. B: Biol. Sci. 353, 113-130.
527 Algeo, T.J., Scheckler, S.E., 2010. Land plant evolution and weathering rates changes in
528 the Devonian. Journal of Earth Science (China University of Geosciences) 21, Suppl.
529 1, 75-78.
530 Algeo, T.J., Berner, R.A., Maynard, J.B., Scheckler, S.E., 1995. Late Devonian oceanic
531 anoxic events and biotic crises: "rooted" in the evolution of vascular land plants. GSA
532 Today 5 (3), 63–66.
533 Andersen, M.B., Romaniello, S., Vance, D., Little, S.H., Herdman, R., Lyons, T.W., 2014.
534 A modern framework for the interpretation of $^{238}U/^{235}U$ in studies of ancient ocean
535 redox. Earth Planet. Sci. Lett. 400, 184–194.
536 Andersen, M.B., Stirling, C.H., Weyer, S., 2017. Uranium isotope fractionation. Rev.
537 Mineral. Geochem. 82, 799-850.
538 Banner, J.L., Hanson, G.N., 1990. Calculation of simultaneous isotopic and trace element
539 variations during water-rock interaction with applications to carbonate diagenesis.
540 Geochim. Cosmochim. Acta 54(11), 3123–3137.
541 Becker, R., Gradstein, F., Hammer, O., 2012. The Devonian period. In: Gradstein, F.M.,
542 Ogg, J.G., Schmitz, M., Ogg, G. (Eds.), The Geologic Time Scale 2012. Elsevier,
543 Amsterdam, pp. 559–601.
544 Becker, R.T., Königshof, P., Brett, C.E., 2016. Devonian climate, sea level and evolutionary
545 events: an introduction. In: Becker, R.T., Königshof, P., Brett, C.E. (Eds.), Devonian
546 Climate, Sea Level and Evolutionary Events. Geological Society, London, Special
547 Publications Vol. 423. pp. 1–11.

548 Berner, R.A., 1997. The rise of plants and their effect on weathering and atmospheric $CO_2$.
549 Science 276 (5312), 544–546.
550 Berner, R.A., Caldeira, K., 1997. The need for mass balance and feedback in the
551 geochemical carbon cycle. Geology 25 (10), 955-956.
552 Berner, R.A., 2006. GEOCARBSULF: a combined model for Phanerozoic atmospheric $O_2$
553 and $CO_2$. Geochim. Cosmochim. Acta 70 (23), 5653–5664.
554 Brand, U., Legrand-Blain, M., Streel, M., 2004. Biochemostratigraphy of the Devonian–
555 Carboniferous boundary global stratotype section and point, Griotte Formation, La
556 Serre, Montagne Noire, France. Palaeogeogr. Palaeoclimatol. Palaeoecol. 205 (3–4),
557 337–357.
558 Caplan, M.L., Bustin, R.M., 1999. Devonian–Carboniferous Hangenberg mass extinction
559 event, widespread organic-rich mudrock and anoxia: causes and consequences.
560 Palaeogeogr. Palaeoclimatol. Palaeoecol. 148 (4), 187–207.
561 Caves, J.K., Jost, A.B., Lau, K.V., Maher, K., 2016. Cenozoic carbon cycle imbalances and
562 a variable weathering feedback. Earth and Planetary Science Letters 450, 152–163.
563 Chen, X., Romaniello, S.J., Herrmann, A.D., Hardisty, D., Gill, B.C., Anbar, A.D., 2018.
564 Diagenetic effects on uranium isotope fractionation in carbonate sediments from the
565 Bahamas. Geochim. Cosmochim. Acta 237, 294–311.
566 Clarkson, M.O., Stirling, C.H., Jenkyns, H.C., Dickson, A.J., Porcelli, D., Moy, C.M.,
567 Pogge von Strandmann, P.A.E., Cooke, I.R., Lenton, T.M., 2018. Uranium isotope
568 evidence for two episodes of deoxygenation during Oceanic Anoxic Event 2. Proc.
569 Natl. Acad. Sci. U.S.A. 115(12), 2918–2923.
570 Cole, D.B., Zhang, S., Planavsky, N.J., 2017. A new estimate of detrital redox-sensitive

571 metal concentrations and variability in fluxes to marine sediments. Geochimica et
572 Cosmochimica Acta 215, 337–353.
573 Dahl, T.W., Boyle, R.A., Canfield, D.E., Connelly, J.N., Gill, B.C., Lenton, T.M., Bizzarro,
574 M., 2014. Uranium isotopes distinguish two geochemically distinct stages during the
575 later Cambrian SPICE event. Earth Planet. Sci. Lett. 401, 313–326.
576 Dahl, T.W., Connelly, J., Li, D., Kouchinsky, A., Gill, B., Porter, S., Maloof, A., Bizzarro,
577 M., submitted. Atmosphere-ocean oxygenation dynamcs during early animal radiation.
578 In review.
579 Dunk, R.M., Mills, R.A., Jenkins, W.J., 2002. A reevaluation of the oceanic uranium budget
580 for the Holocene. Chem. Geol. 190(1-4), 45-67.
581 Henderson, G., Slowey, N., Haddad, G., 1999. Fluid flow through carbonate platforms:
582 constraints from $^{234}U/^{238}U$ and $Cl^-$ in Bahamas pore-waters. Earth Planet. Sci. Lett. 169,
583 99–111.
584 Ingall, E., Jahnke, R., 1994. Evidence for enhanced phosphorus regeneration from marine
585 sediments overlain by oxygen depleted waters. Geochim. Cosmochim. Acta 58 (11),
586 2571–2575.
587 Jacobsen, S.B., Kaufman, A.J., 1999. The Sr, C and O isotopic evolution of Neoproterozoic
588 seawater. Chem. Geol. 161(1–3), 37–57.
589 Joachimski, M.M., Buggisch, W., 2002. Conodont apatite $\delta^{18}O$ signatures indicate climatic
590 cooling as a trigger of the Late Devonian mass extinction. Geology 30 (8), 711–714.
591 Joachimski, M. M., Breisig, S., Buggisch, W., Talent, J. A., Mawson, R., Gereke, M.,
592 Morrow, J. R., Day, J., and Weddige, K., 2009. Devonian climate and reef evolution:
593 Insights from oxygen isotopes in apatite. Earth Planet. Sci. Lett. 284, 599–609.

Johnson, J., Klapper, G., Sandberg, C.A., 1985. Devonian eustatic fluctuations in Euramerica. Geol. Soc. Am. Bull. 96 (5), 567–587.

Kaiser, S.I., Steuber, T., Becker, R.T., Joachimski, M.M., 2006. Geochemical evidence for major environmental change at the Devonian–Carboniferous boundary in the Carnic Alps and the Rhenish Massif. Palaeogeogr. Palaeoclimatol. Palaeoecol. 240 (1–2), 146–160.

Kaiser, S.I., Steuber, T., Becker, R.T., 2008. Environmental change during the Late Famennian and Early Tournaisian (Late Devonian–Early Carboniferous): implications from stable isotopes and conodont biofacies in southern Europe. Geol. J. 43 (2–3), 241–260.

Kaiser, S.I., Becker, R.T., Steuber, T., Aboussalam, S.Z., 2011. Climate-controlled mass extinctions, facies, and sea-level changes around the Devonian–Carboniferous boundary in the eastern Anti-Atlas (SE Morocco). Palaeogeogr. Palaeoclimatol. Palaeoecol. 310 (3–4), 340–364.

Kaiser, S.I., Aretz, M., Becker, R.T., 2016. The global Hangenberg Crisis (Devonian–Carboniferous transition): review of a first-order mass extinction: Geological Society, London, Special Publications 423, 387–437.

Koschinsky, A., Hein, J.R., 2003. Uptake of elements from seawater by ferromanganese crusts: solid-phase associations and seawater speciation. Mar. Geol. 198 (3–4), 331–351.

Lau, K.V., Maher, K., Altiner, D., Kelley, B.M., Kump, L.R., Lehrmann, D.J., Silva-Tamayo, J.C., Weaver, K.L., Yu, M., Payne, J.L., 2016. Marine anoxia and delayed Earth system recovery after the end-Permian extinction. Proc. Natl. Acad. Sci. U.S.A.

617 113(9), 2360–2365.
618 Lau, K.V., Macdonald, F.A., Maher, K., Payne, J.L., 2017. Uranium isotope evidence for
619 temporary ocean oxygenation in the aftermath of the Sturtian Snowball Earth. Earth
620 Planet. Sci. Lett. 458, 282-292.
621 Le Hir, G., Donnadieu, Y., Goddéris, Y., Meyer-Berthaudd, B., Ramstein, G., Blakey, B.C.,
622 2011. The climate change caused by the land plant invasion in the Devonian. Earth
623 Planet. Sci. Lett. 310 (3–4), 203–212.
624 Lenton, T.M., 2001. The role of land plants, phosphorus weathering and fire in the rise and
625 regulation of atmospheric oxygen. Global Change Biol. 7,613–629.
626 Liu, J., Qie, W., Algeo, T.J., Yao, L., Huang, J., Luo, G., 2016. Changes in marine nitrogen
627 fixation and denitrification rates during the end-Devonian mass extinction.
628 Palaeogeogr. Palaeoclimatol. Palaeoecol. 448, 195–206.
629 Liu, J., Luo, G., Lu, Z., Lu, W., Qie, W., Zhang, F., Wang, X., Xie, S., 2018. Shoaling of
630 oxygen minimum zone induced the end Devonian mass extinction. Geochem.
631 Geophys., in press.
632 Marynowski, L., Filipiak, P., 2007. Water column euxinia and wildfire evidence during
633 deposition of the Upper Famennian Hangenberg event horizon from the Holy Cross
634 Mountains (central Poland). Geol. Mag. 144 (3), 569–595.
635 Marynowski, L., Zatoń, M., Rakociński, M., Filipiak, P., Kurkiewicz, S., Pearce, T.J., 2012.
636 Deciphering the upper Famennian Hangenberg Black Shale depositional environments
637 based on multi-proxy record. Palaeogeogr. Palaeoclimatol. Palaeoecol. 346, 66–86.
638 McArthur, J.M., Howarth, R.J., Shields, G.A., 2012. Strontium isotope stratigraphy. In:
639 Gradstein, F.M., Ogg, J.G., Schmitz, M.D., Ogg, G.M., eds., The Geologic Time Scale

2012, Elsevier, Amsterdam, pp. 127–144.

Qie, W., Liu, J., Chen, J., Wang, X., Mii, H.-s., Zhang, X., Huang, X., Yao, L., Algeo, T.J., Luo, G., 2015. Local overprints on the global carbonate $\delta^{13}C$ signal in Devonian–Carboniferous boundary successions of South China. Palaeogeogr. Palaeoclimatol. Palaeoecol. 418, 290–303.

Romaniello, S.J., Herrmann, A.D., Anbar, A.D., 2013. Uranium concentrations and $^{238}U/^{235}U$ isotope ratios in modern carbonates from the Bahamas: Assessing a novel paleoredox proxy. Chem. Geol. 362, 305–316.

Rudnick, R., Gao, S., 2014. Composition of the continental crust. In Treatise on Geochemistry (eds. H. D. Holland and K. K. Turekian), second ed. Elsevier, Oxford, pp. 1–51.

Sallan, L.C., Coates, M.I., 2010. End-Devonian extinction and a bottleneck in the early evolution of modern jawed vertebrates. Proc. Natl. Acad. Sci. U.S.A. 107 (22), 10131–10135.

Schieber, J., 2009. Discovery of agglutinated benthic foraminifera in Devonian black shales and their relevance for the redox state of ancient seas. Palaeogeogr. Palaeoclimatol. Palaeoecol. 271, 292–300.

Scotese, C.R., McKerrow, W.S., 1990. Revised World maps and introduction. In: McKerrow, W.S., Scotese, C.R. (Eds.), Palaeozoic Palaeogeography and Biogeography. Geological Society of London Memoir 12, pp. 1–21.

Tissot, F.L.H., Chen, C., Go, B.M., Naziemiec, M., Healy, G., Bekker, A., Swart, P.K., Dauphas, N., 2018. Controls of eustasy and diagenesis on the $^{238}U/^{235}U$ of carbonates and evolution of the seawater $^{234}U/^{238}U$ during the last 1.4 Myr. Geochim. Cosmochim.

663 Acta 242, 233–265.
664 Tribovillard, N., Averbuch, O., Devleeschouwer, X., Racki, G., Riboulleau, A., 2004. Deep
665 water anoxia over the Frasnian–Famennian boundary (La Serre, France): a tectonically
666 induced oceanic anoxic event? Terra Nova 16, 288–295.
667 Tribovillard, N., Algeo, T.J., Lyons, T., Riboulleau, A., 2006. Trace metals as paleoredox
668 and paleoproductivity proxies: an update. Chem. Geol. 232, 12–32.
669 Veizer, J., Ala, D., Azmy, K., Bruckschen, P., Buhl, D., Bruhn, F., Carden, G.A.F., Diener,
670 A., Ebneth, S., Godderis, Y., Jasper, T., Korte, C., Pawellek, F., Podlaha, O., Strauss,
671 H., 1999. $^{87}Sr/^{86}Sr$, $\delta^{13}C$ and $\delta^{18}O$ evolution of Phanerozoic seawater. Chem. Geol. 161,
672 59–88.
673 Walliser, O.H., 1984. Pleading for a natural D/C boundary. Cour. Forschungsinstitut
674 Senckenberg 67, 241–246.
675 White, D.A., Elrick, M., Romaniello, S., Zhang, F., 2018. Global seawater redox trends
676 during the Late Devonian mass extinction detected using U isotopes of marine
677 limestones. Earth Planet. Sci. Lett. 503, 68–77.
678 Zhang, F., Algeo, T.J., Romaniello, S., Cui, Y., Zhao, L., Chen, Z.Q., Anbar, A.D., 2018a.
679 Congruent Permian-Triassic $\delta^{238}U$ records at Panthalassic and Tethyan sites:
680 Confirmation of global oceanic anoxia and validation of the U-isotope paleoredox
681 proxy. Geology 46(4), 327–330.
682 Zhang, F., Romaniello, S.J., Algeo, T.J., Lau, K.V., Clapham, M.E., Richoz, S., Herrmann,
683 A.D., Smith, H., Horacek, M., Anbar, A.D., 2018b. Multiple episodes of extensive
684 oceanic anoxia linked to global warming and continental weathering following the
685 latest Permian mass extinction. Science Advances 4(4), e1602921.

686 Zhang F., Xiao, S., Kendall, B., Romaniello, S.J., Cui, H., Meyer, M., Gilleaudeau, G.J.,
687 Kaufman, A.J., Anbar, A.D., 2018c. Extensive marine anoxia during the terminal
688 Ediacaran Period. Science Advances 4:eaan8983.
689 Zhang, F., Algeo, T.J., Cui, Y., Shen, J., Song, H.Y., Sano, H., Rowe, H.D., Anbar, A.D.,
690 2019a. Global-ocean redox variation across the Smithian-Spathian boundary linked to
691 concurrent climatic and biotic changes. Earth-Science Reviews 195, 147-168.
692 Zhang, F., Xiao, S., Romaniello, S.J., Hardisty, D., Li, C., Melezhik, V., Pokrovsky, B.,
693 Cheng, M., Shi, W., Lenton, T.M., Anbar, A.D., 2019b. Global marine redox changes
694 drove the rise and fall of the Ediacara biota. Geobiology 17 (6), 594-610.
695
696

## Figures

**Figure 1 Late Devonian paleogeography**. (A) Global paleogeography (modified from Scotese and McKerrow, 1990). The red rectangle represents the area of map B. (B) South China paleogeography (modified from Qie et al., 2015). Study locale is shown by star: LA: Long'an.

**Figure 2 $\delta^{238}U$, $\delta^{13}C_{carb}$, and $\delta^{15}N_{bulk}$ profiles of Long'an section in South China**. L Carbon., Lower Carboniferous; Fm., Formation; Lithol., Lithology; HE, Hangenberg Extinction. P1 and P2 denote positive $\delta^{238}U$ excursions, and N1, N2, and N3 denote negative $\delta^{238}U$ excursions.

**Figure 3 Trace element profiles and elemental ratios of Long'an section**. The orange/blue shaded area denotes horizons affected by sulfidic/anoxic pore-water conditions.

**Figure 4 Mass balance calculations of fraction of uranium removal to anoxic sinks based on diagenetic offsets ($\Delta_{offset}$) of 0‰, 0.27‰, and 0.3‰. Two independent calculations using fractionation factors between seawater and anoxic sinks of 0.6‰ and 0.85‰, respectively, are shown for comparison.**

**Figure 5 U isotope model estimates of local versus global expansion of marine anoxia.** In model scenario 1 (MS1), anoxic marine areas initially started from an oxygenated ocean

similar to the modern-day, which started to expand at peak of P1. The local anoxia in the model is assumed to be proportional to the $\Delta_{offset}$ that can be generated between average carbonates and anoxic carbonates. The $\Delta_{offset}$ varies between 0.27‰ and 0.6‰. The model scenario 2 (MS2) started from a situation similar to that in MS1 but expanded prior to peak of P1 and further expanded between P1 and N2.

**Figure 6 Distribution of $\Delta_{offset}$ ($\delta^{238}U_{carbonate}$- $\delta^{238}U_{seawater}$) in model scenario 1, model scenario 2, and CPU model (Fig. 7) for Long'an compared to modern carbonates**. In model scenario 1, the average $\Delta_{offset}$ is similar to that of modern carbonates but the Long'an section displays more scatter. In model scenario 2, both the average $\Delta_{offset}$ value and its variability is greater for the Long'an section than observed in modern carbonates.

**Figure 7 Global C, P, U model scenario of increased land plant cover and enhanced continental weathering as a cause of coupled global changes.** (A) Model scenario of a 33% increase in plant cover (V) and associated bulk weathering amplification (W) over 200 kyr starting at 359.28 Ma, and resulting response of normalized P content of ocean ($P/P_0$), anoxic fraction of ocean ($f_{anoxic}$), $CO_2$ (PAL), $\delta^{13}C$ (‰), normalized U content of ocean ($U/U_0$), and $\delta^{238}U_{sw}$ (‰). (B) Comparison of data (symbols), running mean of data (red line), and modelled $\delta^{238}U_{sw}$ (blue line), assuming a fixed offset (0.27‰) of $\delta^{238}U_{carb}$ from seawater $\delta^{238}U$ (green line), and maximum $\delta^{238}U_{carb}$ assuming a maximum offset of 0.6‰ from seawater (purple line). (Note the shift in the time axis between panels A and B.)

743 Figure 1

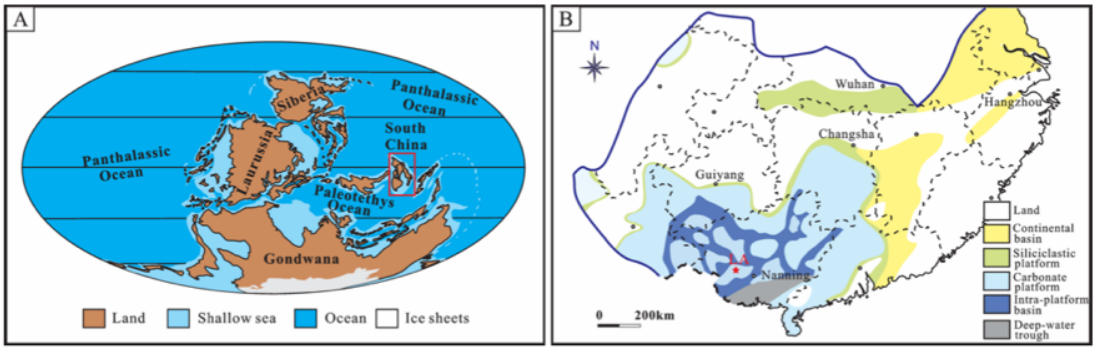


744

745

746

747 Figure 2

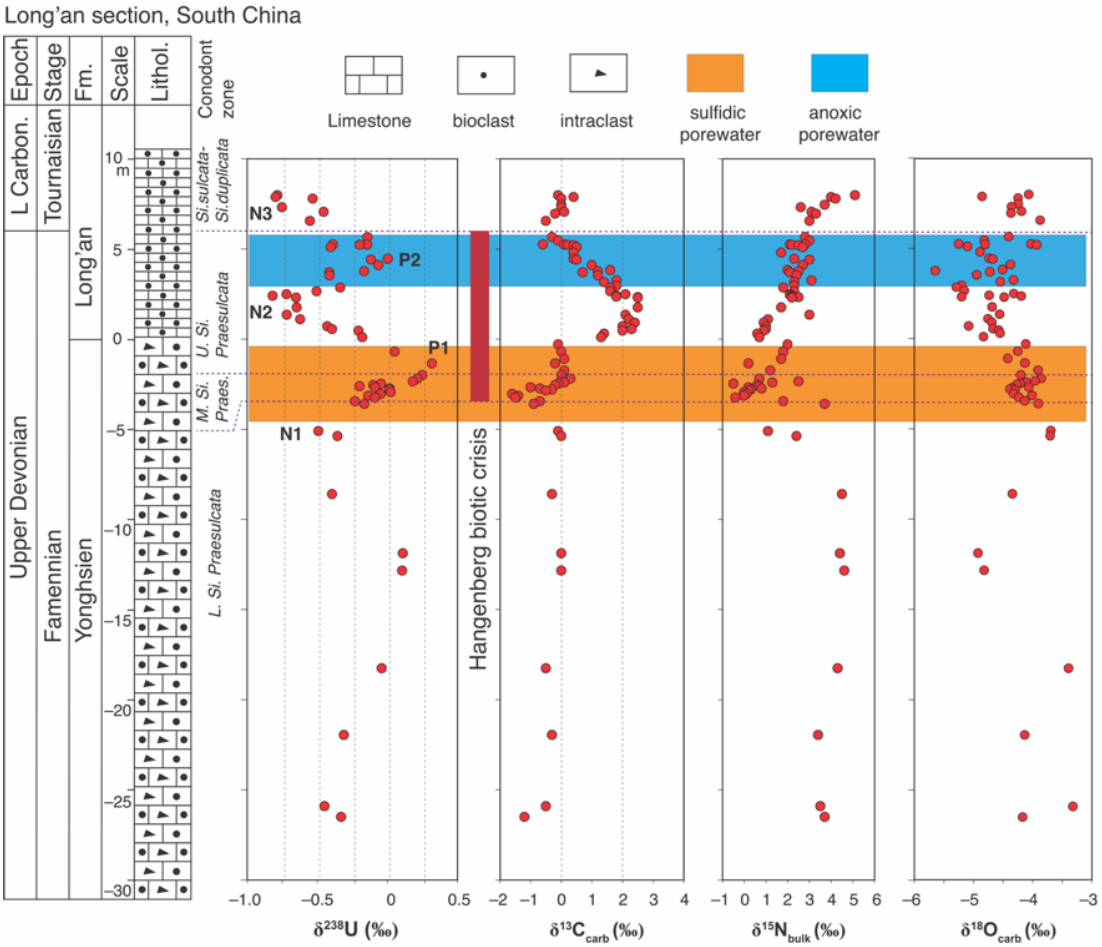


748

749

750

751

752 Figure 3

753

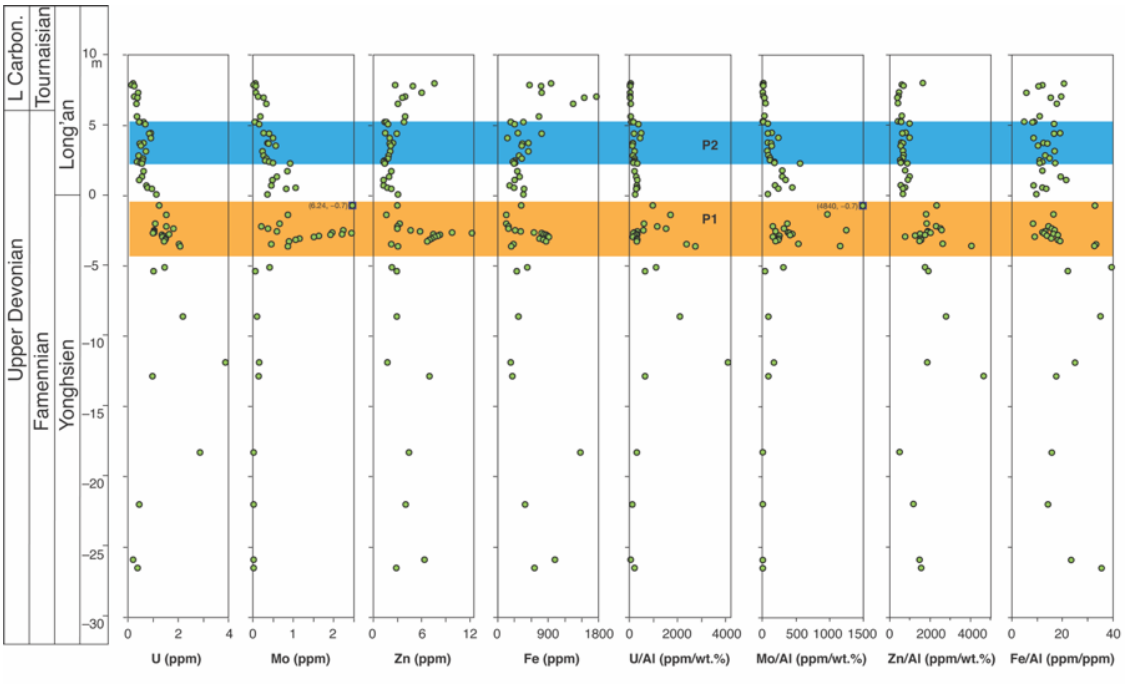


754

755 Figure 4

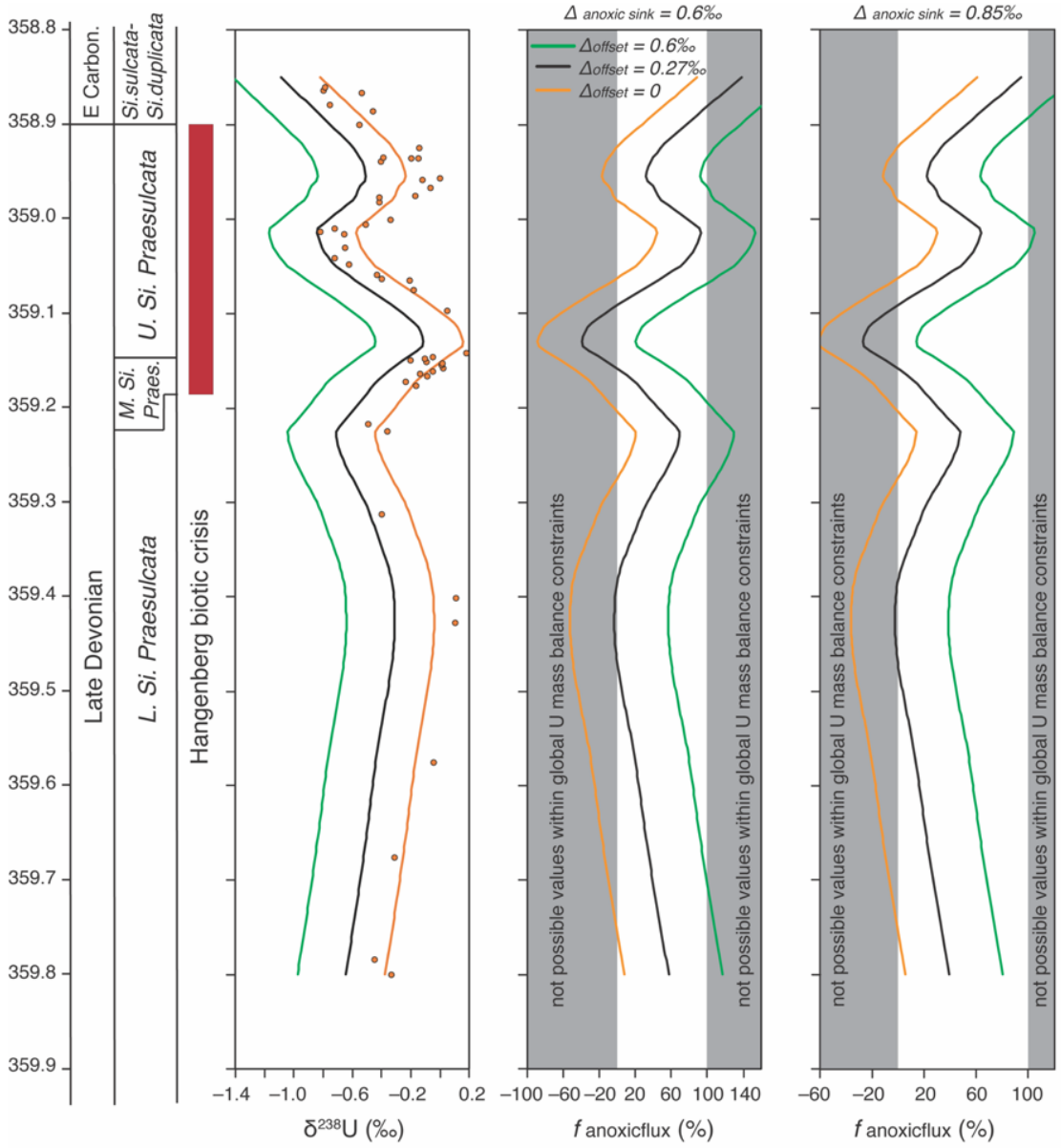


756

757 Figure 5

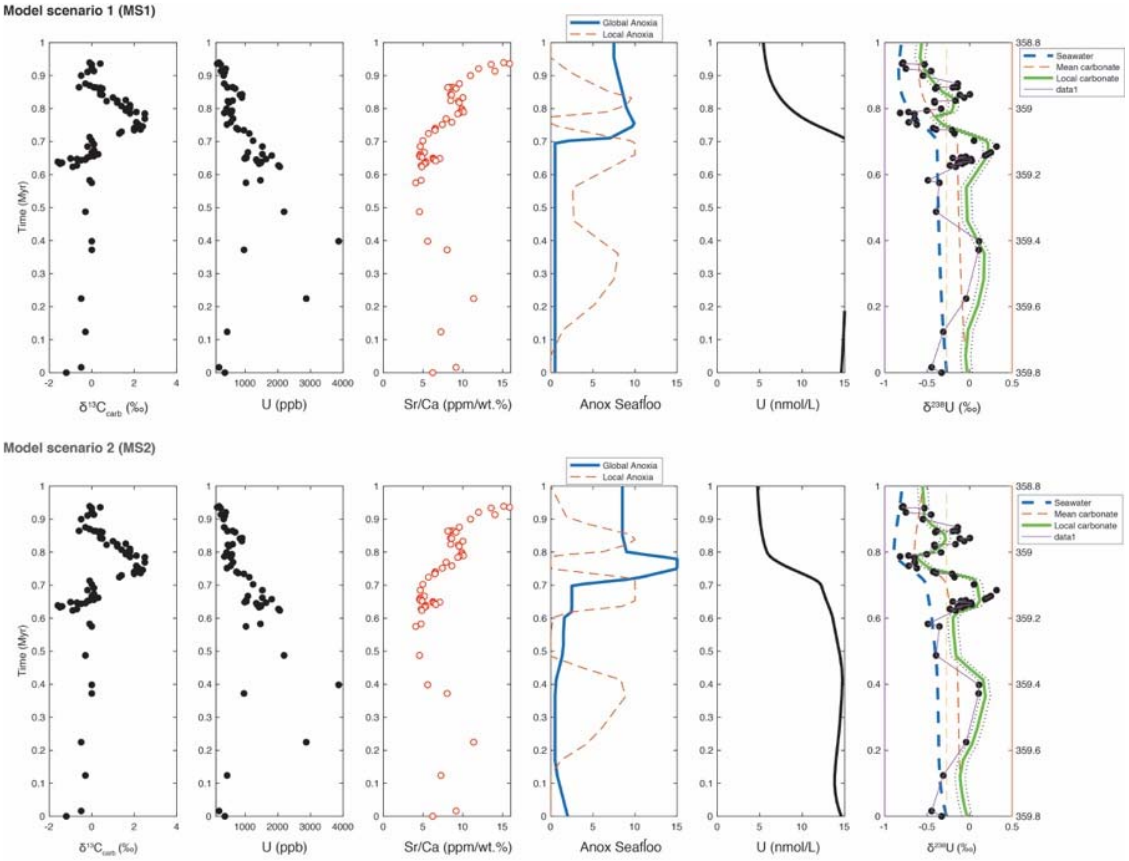


758

759

760

761

762

763 Figure 6

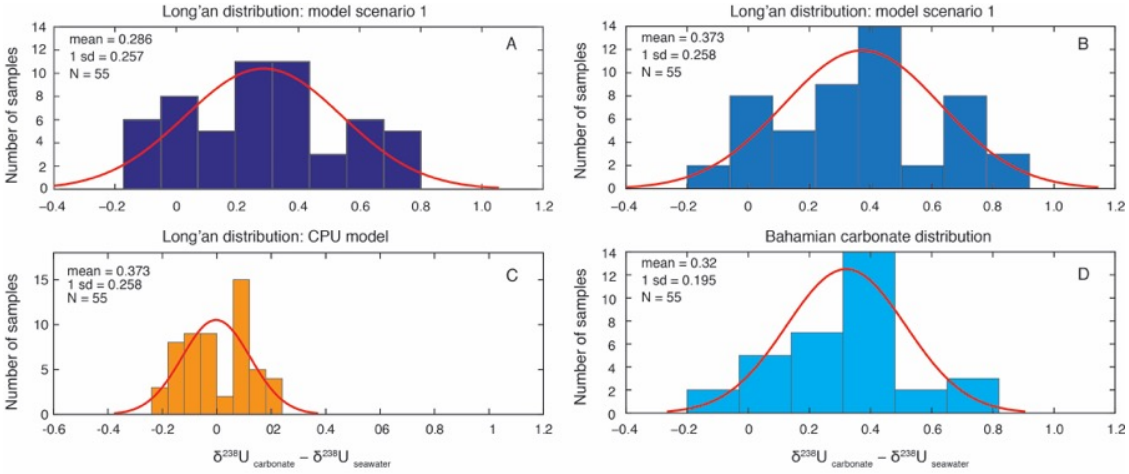


764

765

766

767 Figure 7
768

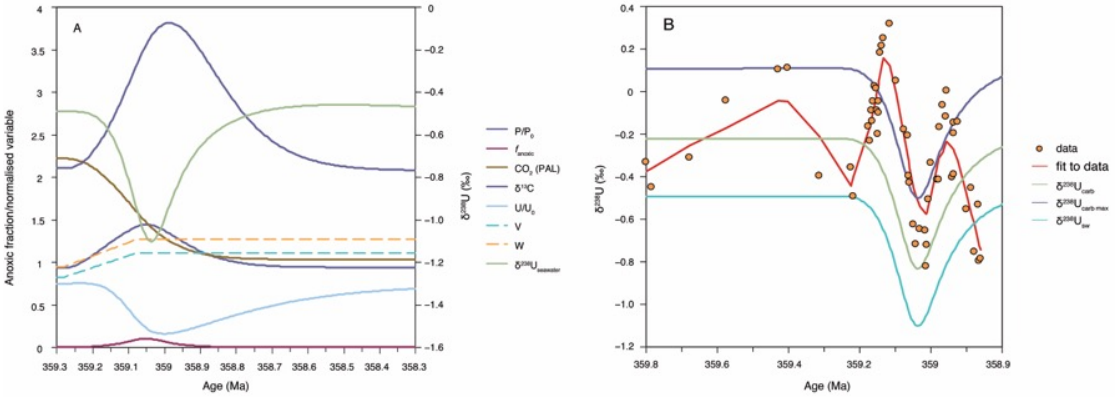


769
770
771

772
773 **Table 1 Uranium box model parameterization.**

| Model parameters | | Modern | | Reference |
|---|---|---|---|---|
| Ocean volume | $V_{ocean}$ | 1.30E+21 | L | |
| Oceanic U inventory | $N_{sw}$ | 1.90E+13 | mol | |
| Anoxic seafloor area | $A_{anoxic}$ | 0.5% | (% of total seafloor) | |
| <u>Fluxes</u> | | | | |
| Oceanic input flux (rivers, groundwater, aeolian) | $J_{river}$ | 5.30E+7 | mol/yr | Dunk et al., 2002 |
| Sediment burial flux in anoxic settings | $J_{anoxic}$ | 1.17E+7 | mol/yr | Dunk et al., 2002 |
| Sediment burial flux in other settings | $J_{other}$ | 4.64E+7 | mol/yr | Dunk et al., 2002 |
| **Uranium isotope cycle** | | | | |
| Uranium isotope composition of oceanic input | $\delta^{238}U_{river}$ | −0.27 | ‰ | Andersen et al., 2017 |
| Uranium isotope difference between buried anoxic sediments and seawater | $\Delta^{238}U_{anoxic}$ | +0.60 | ‰ | Andersen et al., 2017 |
| Uranium isotope difference between buried other sediments and seawater | $\Delta^{238}U_{other}$ | +0.05 | ‰ | Dahl et al., 2014 |
| Uranium isotope difference between carbonates and seawater | $\Delta^{238}U_{carb}$ | +0.24 | ‰ | Chen et al., 2018 |
| Maximal U isotope offset in carbonates | $\Delta_{offset,\ maz}$ | +0.60 | ‰ | Romaniello et al., 2013 |
| Local conditions at Long'an | $\Delta_{offset}$ | change with time | ‰ | |

774
775
776
777